ACS OMEGA

http://pubs.acs.org/journal/acsodf

Article

Mechanochemical Synthesis and Magnetic Characterization of Nanosized Cubic Spinel $FeCr_2S_4$ Particles

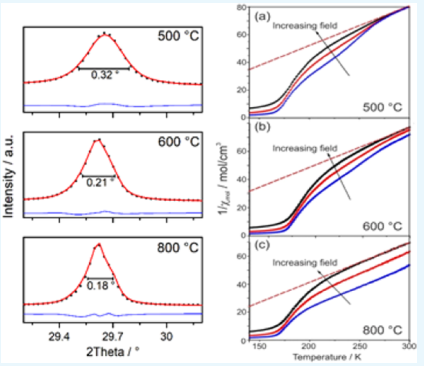
Anna-Lena Hansen, Reinhard K. Kremer,* Eva M. Heppke, Martin Lerch, and Wolfgang Bensch*

Cite This: *ACS Omega* 2021, 6, 13375−13383

Read Online

ACCESS | Metrics & More | Article Recommendations

ABSTRACT: Nanosized samples of the cubic thiospinel $FeCr_2S_4$ were synthesized by ball milling of FeS and Cr_2S_3 precursors followed by a distinct temperature treatment between 500 and 800 °C. Depending on the applied temperature, volume weighted mean (L_{vol}) particle sizes of 56 nm (500 °C), 86 nm (600 °C), and 123 nm (800 °C) were obtained. All samples show a transition into the ferrimagnetic state at a Curie temperature T_C of ∼ 167 K only slightly depending on the annealing temperature. Above T_C, ferromagnetic spin clusters survive and Curie−Weiss behavior is observed only at $T \gg T_C$, with T depending on the heat treatments and the external magnetic field applied. Zero-field-cooled and field-cooled magnetic susceptibilities diverge significantly below T_C in contrast to what is observed for conventionally solid-state-prepared polycrystalline samples. In the low-temperature region, all samples show a transition into the orbital ordered state at about 9 K, which is more pronounced for the samples heated to higher temperatures. This observation is a clear indication that the cation disorder is very low because a pronounced disorder would suppress this magnetic transition. The unusual magnetic properties of the samples at low temperatures and different external magnetic fields can be clearly related to different factors like structural microstrain and magnetocrystalline anisotropy.



INTRODUCTION

Binary and ternary chromium chalcogenides exhibit a large variety of chemical and physical properties explaining the intense research of these materials. Examples for the diversity of properties are a large linear negative thermal expansion,[1] the tuneable thermoelectric properties,[2−5] a large magnetocaloric effect,[6] the photocatalytic properties in dye degradation,[7] the tuning of magnetic properties by Li intercalation,[8] ferrimagnetic properties in nanosheets,[9] the application as stable electrode material in sodium-ion batteries,[10] or the generation of nanoscale networks.[11] One of the most intensely investigated ternary chromium chalcogenides is the iron chromium thiospinel $FeCr_2S_4$, which crystallizes in the normal cubic spinel structure with the general formula AB_2X_4 (space group: *Fd*3*m*, no. 227). The S^{2-} anions are arranged in a close-packed face-centered cubic (fcc) lattice, creating tetrahedral (A) and octahedral (B) voids, which are partially occupied by the Fe and Cr cations. The Fe^{2+} cations occupy 1/8 of the tetrahedral voids and the Cr^{3+} cation 1/2 of the octahedral positions. The d-orbitals of the Fe^{2+} cations are split into an energetically lower *e* doublet and an upper t_2 triplet. The $3d^6$ electrons are distributed over the orbitals according to Hund's rule, yielding a high-spin configuration with $S = 2$, and these cations are Jahn−Teller active. The $3d^3$ electrons of the Cr^{3+} cations occupy the t_{2g} level with $S = 3/2$. The magnetic and especially the magnetoelectric properties of $FeCr_2S_4$ attracted particular attention.[12−14] Three main exchange couplings affect the magnetic behavior of $FeCr_2S_4$: nearest-neighbor ferromagnetic B−B (Cr−Cr) interactions, the more distant neighbor antiferromagnetic B−B interactions, and the 120° A−B superexchange interaction that is antiferromagnetic. By neutron powder diffraction, $FeCr_2S_4$ has been shown to order ferrimagnetically below ∼180 K with Fe and Cr moments aligned collinear antiparallel.[15] Already early on unusual physical properties like a complex behavior of the Hall resistivity,[16] anisotropic resistivity and magnetoresistance effects due to spin disorder were reported.[17] Mössbauer spectroscopic investigations on polycrystalline $FeCr_2S_4$ demonstrated an unusual behavior of the electric field gradient at the Fe^{2+} site at about 10 K.[18,19] Further, low-temperature Mössbauer spectroscopy studies indicated a static cooperative Jahn−Teller (JT) distortion ($c/a < 1$) on the tetrahedral site, stabilizing the ^5E_g ground state of the Fe^{2+} cations.[20−22] Heat capacity measurements at low temperatures exhibited a λ-like anomaly around this temperature but the particular shape of this anomaly depends on the stoichiometry of the sample.[23,24]

Received: March 16, 2021
Accepted: April 20, 2021
Published: May 10, 2021



Downloaded via 83.236.27.156 on October 27, 2021 at 07:51:19 (UTC).
See https://pubs.acs.org/sharingguidelines for options on how to legitimately share published articles.

ACS Publications

© 2021 The Authors. Published by American Chemical Society

Colossal magnetoresistance (CMR) behavior was observed with a magnitude comparable to that found in manganites.[25] However, adverse to the manganites, the CMR is not caused by double exchange or a JT distortion.[26,27] It was proposed that by increasing the temperature, long-range magnetic order gradually breaks down by approaching T_C accompanied by the formation of nanosized spin clusters, which survive well above T_C. In an external magnetic field above T_C, the rapidly fluctuating spin clusters coalesce and generate bulk-like ferromagnetism, which leads to the lowering of electrical resistivity. Evidence for superexchange interactions between Fe^{2+} and Cr^{3+} cations in $FeCr_2S_4$ was obtained using resonant inelastic X-ray scattering (RIXS) investigations.[28]

Below the Curie temperature T_C, which varies between 177[29] and 167 K,[30−32] several unusual features were observed in the temperature-dependent magnetization curves: A cusp-like anomaly occurs at $T_m \sim 60$ K as well as a splitting of the *zfc*−*fc* susceptibility data below this temperature.[30,33−35] The divergence of the *zfc*−*fc* susceptibilities resembles a glassy behavior, which is exceptional for a stoichiometric and ordered system. Spin-glass-like states were also postulated to exist below 60 K due to fluctuating competing exchange interactions in conjunction with high magnetocrystalline anisotropy for the Fe^{2+} moments at the tetrahedral site being strongly antiferromagnetically coupled with Cr^{3+} cations.[33] This unusual magnetic behavior was attributed to changes in the domain structure[30] and the appearance of noncubic magneto-crystalline anisotropy.[36] The latter was proposed to be the result of the structure transformation, generating pinning centers for magnetic domain walls. But neutron scattering investigations demonstrated that the magnetic structure is of simple Néel type well down to 4 K with $\mu(Cr) = 2.9\ \mu_B$ and $\mu(Fe) = 4.2\ \mu_B$, giving a total magnetic moment $\mu = 1.6\ \mu_B$ (T_C = 180 K).[37] In other neutron diffraction studies, the values 1.92 μ_B/fu (fu = formula unit)[38] and 1.59 μ_B/fu were determined.[12] A broadening of Bragg reflections in X-ray powder diffraction patterns below T_C was attributed to inhomogeneous lattice distortions.[39] Low-temperature high-resolution transmission electron microscopy on oriented single crystals of $FeCr_2S_4$ showed a cubic to triclinic structural phase transition within crystallographic domains and an overall symmetry reduction from $Fd3m$ to $F\bar{4}3m$.[40] The proposed structural transformation at $T_m \approx 60$ K could be revealed with ultrasonic measurements on single crystals.[41] An anomaly in the magnetization versus field curve was observed for $\mu_0 H$ = 5.5 T, which was attributed to the development of a new magnetic phase, most probably from the incommensurate noncollinear spin structure[42] to the commensurate collinear spin structure.[43] Spin reorientation at 60 K was also reported from ultrasound studies on dense polycrystalline samples.[44] ac magnetic susceptibility measurements performed on oriented single crystals showed a pronounced frequency dependence between 90 and 20 K for both the real and imaginary parts of the ac susceptibility. The observations made for the field and temperature dependence were explained by domain wall pinning. Below 60 K, changes in the domain structure and appearance of pinning centers caused by structural changes were suggested to lead to spin-glass-like magnetic anomalies below 60 K.[30]

A second anomaly in the magnetic susceptibility data was observed at around 9 K and attributed to orbital ordering.[18,19,38,45−47] It was argued that this anomaly occurs due to a unit cell volume contraction and that a cooperative JT effect and spin−orbit coupling of the Fe^{2+} ion compete, leading to spin reorientation at about 60 K, which gives rise to the onset of short-range orbital ordering at this temperature.[48] It is noteworthy that the anomaly at $T \sim 9$ K can be suppressed in polycrystalline specimens by applying large magnetic fields.[49] For single crystals, experimental evidence was presented that an orbital glass phase is formed at $T_{OO} \sim 9$ K.[32,33,35,42,43,47] The Curie temperature and the anomaly at 9 K are only weakly shifted at high external fields up to 9 T. At lower magnetic fields, the magnetic moments of Fe^{2+} and Cr^{3+} are lower than the spin-only values, and only for $\mu_0 H_{ext}$ = 5.5 T, the expected spin-only values are reached. The dielectric permeability shows a linear correlation with the magnetization of the sample, which is consistent with the existence of ferroelectric polarization and a multiferroic ground state below 10 K.[12,13] The critical exponents, β, γ, and δ, for the paramagnetic to ferrimagnetic phase transition were determined using different approaches. β and γ are found close to the mean field theory values, whereas δ is higher than expected, which has been attributed to incomplete ferrimagnetic transition and the presence of short-range ordering above T_C.[31]

A perpetual problem with $FeCr_2S_4$ samples, crystals and polycrystalline material, is that often the physical properties depend essentially on the detailed synthesis conditions, causing hardly controllable minute compositional mismatch and/or positional disorder of the cations. Consequently, samples synthesized by conventional high-temperature techniques often showed differences in the magnetization and *zfc*−*fc* curves compared to, e.g., a material obtained by the field-activated sintering technique (FAST). However, for the FAST sample, the magnetic anomaly at $T_{OO} \sim 9$ K was found absent and the anomaly normally occurring at $T_m \sim 60$ K is shifted to a lower temperature. In addition, the transition from paramagnetic to the ferrimagnetic state is less sharp for the FAST sample. All observations have been attributed to residual structural disorder in the samples prepared with FAST.[50] To summarize, the magnetic characteristics of single-crystalline and polycrystalline $FeCr_2S_4$ samples are as follows: (i) a transition from paramagnetic to the ferrimagnetic state occurs at $T_C \sim 170$ K; (ii) below the Curie temperature, structural changes or lattice distortions as well as spin reorientation set in, leading to magnetic anomalies at about 60 K; and (iii) orbital ordering is observed at $T_{OO} \approx 9$ K.

In the past, all investigations were performed on well-crystallized polycrystalline samples of $FeCr_2S_4$ or on single crystals, which were prepared by chemical vapor deposition. The only exception is the study of FAST samples reported in ref 50, which showed a different magnetic behavior compared to single crystals or microcrystalline samples. A systematic study of the changes of the magnetic behavior as a function of sizes of coherently scattering domains was not performed until now on $FeCr_2S_4$. For the preparation of nanoparticles, several synthetic approaches were well established. Very often solvent-mediated methods are applied, which have the disadvantage that the surfaces of the crystallites are covered by capping molecules. To avoid such impurities, mechanochemistry is a promising approach. While this synthetic approach is applied in many areas of inorganic and organic chemistry, it has rarely been utilized for the preparation of ternary sulfides. Hence, we decided using the mechanochemical technique for the first time for the generation of nanosized $FeCr_2S_4$ materials. The main aim of the present study is to get better insights into the variation of the magnetic properties in the nanoregime and

https://doi.org/10.1021/acsomega.1c01412
ACS Omega 2021, 6, 13375−13383

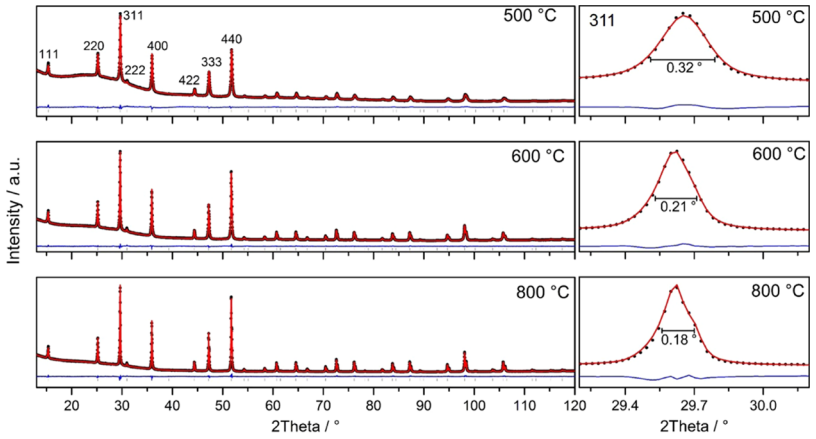


Figure 1. Results of the Rietveld refinements of the powder patterns of the three samples. Bragg indices of some prominent reflections are given. Black: collected data; red: refined data; and blue: difference curves. The vertical bars indicate the positions of Bragg reflections used to calculate the patterns. The insets show an enlarged view of the 311 reflection.

therefore we intentionally synthesized nanosized $FeCr_2S_4$ polycrystalline samples with particle size distributions ranging between 10 and 50 nm by reacting ball-milled mixtures of FeS and Cr_2S_3 at temperatures between 500 and 800 °C. With increasing annealing temperature, we find a continuous increase of the particle size, a moderate increase of saturation magnetic moment, and a variation of magnetocrystalline anisotropy. We attribute these observations to the variation of the defect structure with the annealing temperature modifying the approach to magnetic saturation.

RESULTS AND DISCUSSION

Particle Size. The XRPD patterns of the three samples and the results of the Rietveld refinements assuming the space group *Fd*3*m* (no. 227) (Fe: 8a; Cr: 16d; S: 32e, 0.383) are displayed in Figure 1. All samples are phase pure and the cubic lattice parameters were refined to 9.9832(1) Å (500 °C), 9.9922(1) Å (600 °C), and 9.9923(1) Å (800 °C). The cubic lattice parameter *a* of the 500 °C sample is significantly smaller than values reported in the literature. There data scattering in a very narrow band around 10 Å[13,50−55] can be found, while in ref 33, the authors obtained *a* = 9.983 Å for one sample, mentioning that the lattice parameter depends on the stoichiometry, but unfortunately the exact composition was not reported. Even for a sample with crystallite sizes between 40 and 45 nm, *a* was determined to 10.008(1) Å.[50] We note that the cubic lattice parameter *a* is significantly reduced at low temperatures, from 9.9894(3) Å at 180 K to 9.9808(3) Å at 5 K.[48] In a further study, a decrease from 9.9813(3) Å (175 K) to 9.9756(3) Å (10 K) was reported.[38]

Increasing the annealing temperature of our samples has two effects revealed by the XRPD patterns:

1. The broad bulge below ∼30° in 2θ decreases significantly in intensity and almost vanishes for the 800 °C sample, which is assigned to a reduction of incoherently scattering defects.
2. As demonstrated for the 311 Bragg reflections (the right side of Figure 1), increasing the annealing temperature leads to a linewidth reduction, indicating an increase in the sizes of coherently scattering domains.

This effect is also clearly seen in the parameters of fitted log-normal distribution of the coherently scattering domains (Figure 2). The mean particle size value μ and the variance σ

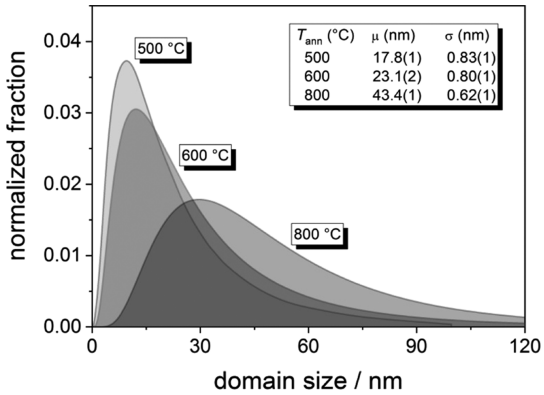


Figure 2. Size distribution of the coherently scattering domains analyzed from the XRPD patterns according to eq 3 as a function of annealing temperature, as indicated. The shaded areas indicate log-normal distributions with parameters given in the inset.

vary continuously with the annealing temperature. Whereas μ increases by more than a factor of 2, σ decreases as shown in Figure 3. The volume weighted mean (L_{vol}) increases from 56 nm (500 °C) to 86 nm (600 °C) ending at 123 nm for the sample heated at 800 °C.

The strain values ε_0 obtained from the Rietveld refinements decrease with the annealing temperature from 7.4×10^{-4} (500

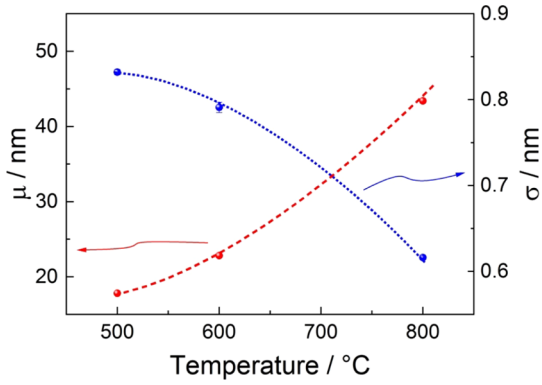


Figure 3. Mean value μ and variance σ of the log-normal distributions (eq 3) of the coherently scattering domains as a function of annealing temperature.

https://doi.org/10.1021/acsomega.1c01412
ACS Omega 2021, 6, 13375−13383

°C) to 1.8 × 10^{-4} (600 °C) to finally reach 9 × 10^{-5} for the samples annealed at 800 °C. The smaller value for the lattice parameter of the sample prepared at 500 °C may be caused by the larger number of nanocrystallites compared to the materials heated at higher temperatures. In the literature, mainly a lattice expansion was reported for oxides even for particles larger than 100 nm,[56] while a lattice contraction was observed for metallic nanoparticles.[57] However, there are also observations that the lattice contracts with decreasing particle size, e.g., for α-Fe_2O_3.[58] This phenomenon was explained by an increased covalency of the Fe−O bond on the nanoscale. Because the Cr−S and Fe−S bonds are much more covalent than in oxides, we assume that the unit cell contraction is based on a similar phenomenon.

Magnetic Properties. Figure 4 displays the inverse magnetic susceptibilities collected at 1, 2, and 4 T. At sufficiently high temperatures and significantly above the Curie temperature, the inverse susceptibilities converge to Curie−Weiss behavior with the same slope for all three samples similar to that observed by Gibart et al.[29] On approaching the ferrimagnetic Curie temperature, the susceptibilities become field-dependent with the largest field splitting seen for the 800 °C sample. We attribute this splitting to ferrimagnetic spin clusters, which can be saturated with increasing field, leading to an increase of the inverse susceptibilities with larger measuring fields.

For all samples, a transition to the ferrimagnetic state is determined at T_C ∼ 167 K, in agreement with the literature where values between 177[29] and 167 K were reported.[30−32] Bifurcation of the *zfc*−*fc* data occurs at 120, 110, and 100 K (Figure 5) for the samples prepared at 500, 600, and 800 °C, respectively. Below the bifurcation, the *zfc* curves continuously decrease and settle into a plateau below ∼25 K. A clear step-like drop of the magnetic susceptibility occurs at ∼9 K for the 800 and 600 °C samples, which is caused by the long-range orbital ordering as discussed in the literature. This anomaly is less well developed for the sample prepared at 500 °C. The decrease of the *zfc* susceptibility with decreasing temperature can be attributed to microscopic modifications in the long-range ordered magnetic structure and/or different magneto-crystalline anisotropy due to varying amounts of structural defects, affecting the temperature dependence of the domain dynamics. Notable is the different behavior of the samples. Whereas for the 800 °C sample, "melting" of the domain structure on approaching from low temperatures starts at about 50 K, a sizeable increase of the *zfc* susceptibility of the 500 °C sample begins only at about 75 K, indicating more effective domain pinning. Below the bifurcation and before settling into saturation, the *fc* susceptibilities pass through shallow maxima, most pronounced for the 800 °C sample.

Figure 6 displays magnetization curves collected at 4 K in external fields up to 9 T. The saturated moment increases with the preparation temperature from 1.76 μ_B, 1.80 μ_B, to 1.83 μ_B at 9 T for the 500, 600, and 800 °C samples, respectively. For the collinear ferrimagnetic structure, a saturated magnetic moment of 1.6 μ_B was reported from high-magnetic-field experiments.[43] DFT-based calculations predicted saturation values of 2.0 μ_B[59] and 1.92 μ_B.[60] For polycrystalline compounds, the data reported in the literature are, e.g., 1.55 μ_B given in ref 60 or ∼1.6 μ_B reported in refs 12, 37. For the

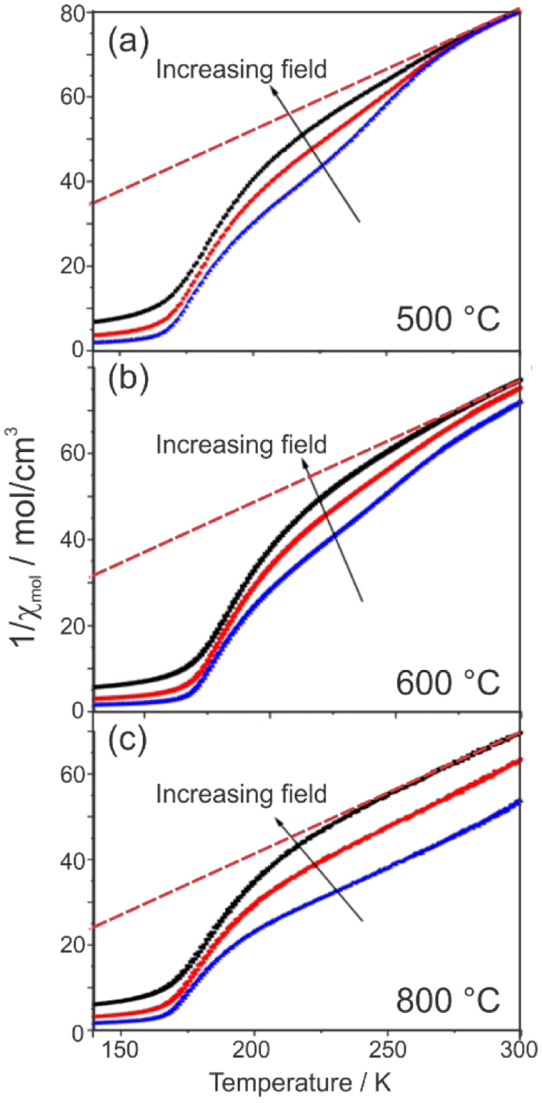


Figure 4. Inverse molar magnetic susceptibilities of the three $FeCr_2S_4$ samples prepared at different temperatures: (a) 500 °C, (b) 600 °C, and (c) 800 °C. Blue, red, and black colored traces refer to data collected at 1, 2, and 4 T, respectively. The dashed lines indicate Curie−Weiss laws approaching the high-temperature behavior of the data collected at 4 T.

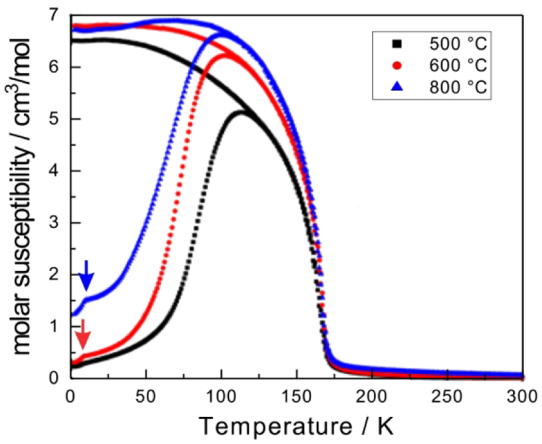


Figure 5. *zfc*−*fc* magnetic susceptibilities measured at 0.1 T. The arrows mark the transition into the orbital ordered state at ∼9 K.

https://doi.org/10.1021/acsomega.1c01412
ACS Omega 2021, 6, 13375−13383

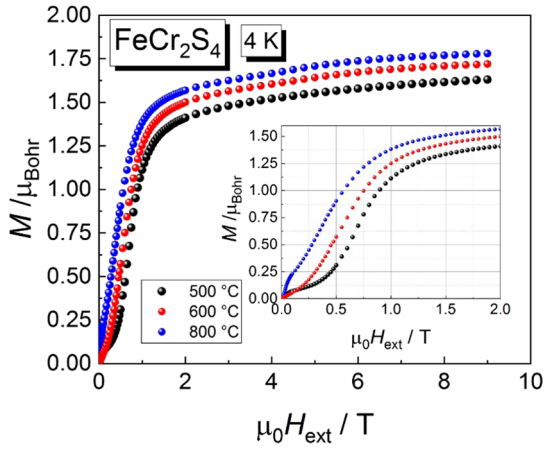


Figure 6. Magnetization at 4 K of the three samples prepared at 500, 600, and 800 °C, as indicated. The inset displays an enlarged view of the low-field regime.

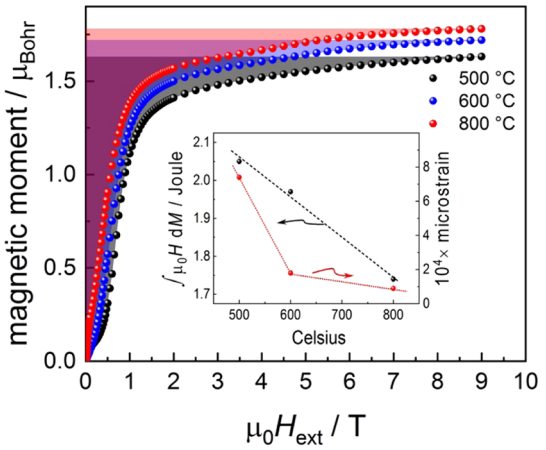


Figure 7. Magnetic moment per fu as a function of external magnetic field at 4 K. The shaded areas highlight the integral $\int \mu_0 H\, dM'$. The inset displays the integral $\int_0^{M_{sat}} \mu_0 H(M')\, dM'$ (black dots) corresponding to the color shaded areas in the main frame and the microstrain (red dots, see the text above) as a function of preparation temperatures of the three samples prepared at the temperatures, as indicated. The dashed and dotted lines in the inset are guides to the eye.

samples investigated here, the values are noticeably larger but do not fully reach the theoretically predicted values. The increase of the magnetic moment with the annealing temperature may be explained by reduced surface spin canting, a smaller magnetic dead-layer and/or a reduced number of defects on the Cr and Fe sublattices. One may speculate that the larger values obtained here are caused by an imperfect collinear magnetic structure, which may be due to microstrain that is significantly reduced with increasing annealing temperature (see above). We note that the saturation value of the sample annealed at 800 °C matches that measured on a single crystal for the <111> direction (1.84 μ_B), which is the hard magnetic axis.[33]

Also apparent from the magnetization curves is the difference in the behavior at small fields where domain wall motions are the prevailing process of magnetization. For the 800 °C sample, magnetization grows rapidly, whereas for the 500 °C sample, after a pedestal at low fields, the magnetization increases with about the same slope as for the other samples. The magnetization behavior reflecting domain wall motion at low fields correlates with the magnitude of the microstrain derived from the XRPD measurements. The different magnetization versus field behavior at low temperatures can be attributed to varying crystalline anisotropy energies for the different samples.

The work $W(M)$ done when magnetizing to a certain field $\mu_0 H$ is given by the area between the M–H curve and the magnetization axis. It can be obtained by integration according to[61]

$$W(M) = \int_0^M H(M')\, dM' \tag{1}$$

For cubic crystals, the anisotropy energy is usually described by the three anisotropy coefficients K_i (i = 0, 1, 2), which weighs the products of even powers of the directional cosines measured with respect to the distinguished magnetization axes system. For a polycrystalline sample with a random orientation of the crystallites with respect to the external field, the anisotropy work W can only be taken as a qualitative measure of the anisotropy energy. Integration of the area of the 4 K magnetization curves, as indicated by the shaded areas in Figure 7, indicates that the anisotropy energy (see the inset of Figure 7) decreases with increasing preparation temperature by about 15%, paralleling the decrease of the microstrain for higher preparation temperatures. In addition, higher preparation temperatures appear to reduce imperfections in the samples and the crystal anisotropy.

The magnetization of the samples was recorded at different temperatures up to T = 175 K somewhat higher than T_C (Figure 8). As expected, the magnetic moment obtained at the highest magnetic field decreases with increasing temperature. But even at 175 K, the magnetization is not linear as expected for a paramagnetic material, and a magnetic moment of ≈0.75 μ_B is observed for all samples, which is again an indication for the presence of spin clusters, which survived at $T > T_C$.

At sufficiently high fields (see Figure 8) in the regime where magnetization processes by domain rotation ($\mu_0 H \gtrsim 2$ T) prevail, it has been found that the field dependence of the magnetization provides information about the type of defects in the sample ("law of approach").[61−65] Generally, the approach to saturation is expanded in a polynomial of powers of the inverse magnetic field according to

$$M(H) = M_{sat}\,(1 - a_1/(\mu_0 H) - a_2/(\mu_0 H)^2 - \cdots) + a_0\,\mu_0 H \tag{2}$$

The coefficient a_1 is interpreted to describe inclusions and/or microstress and a_2 is due to crystal anisotropy. At temperatures well below the Curie temperature, the term $a_0\mu_0 H$, which represents the field-induced increase in the spontaneous magnetization of the domains or forced magnetization, is usually very small and neglected. A plot of the magnetization of the three $FeCr_2S_4$ samples as a function of inverse external field (Figure 8), $1/\mu_0 H$, shows that the magnetizations at 4 K for very high fields follow very well straight lines with no significant slope change. Considering the field range from 0.5 to 9 T and fitting the experimental data to eq 2 reveals that the deviations toward lower fields can be favorably taken care of by additionally considering the term ∝ $1/(\mu_0 H)^2$, as displayed in Figure 9.

https://doi.org/10.1021/acsomega.1c01412
ACS Omega 2021, 6, 13375−13383

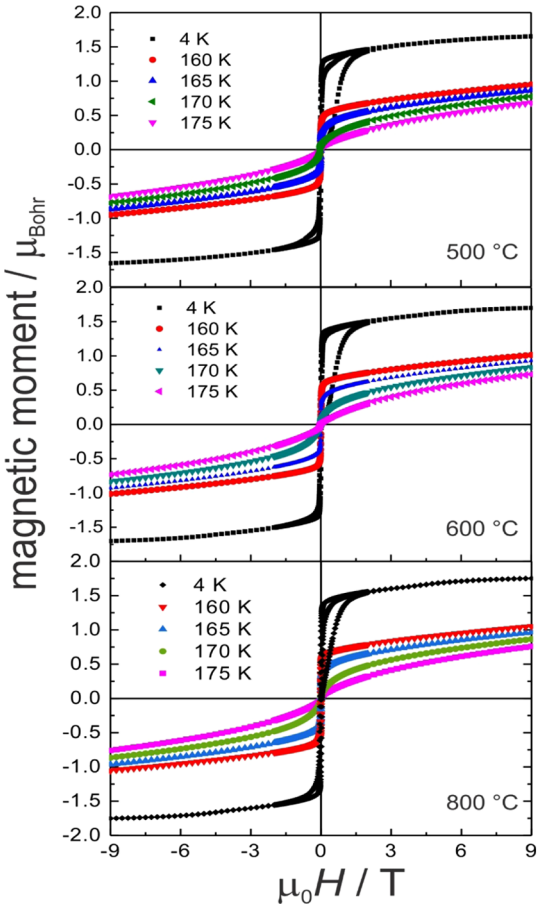


Figure 8. Magnetization (per fu) of the 500, 600, and 800 °C samples recorded at different temperatures, as indicated.

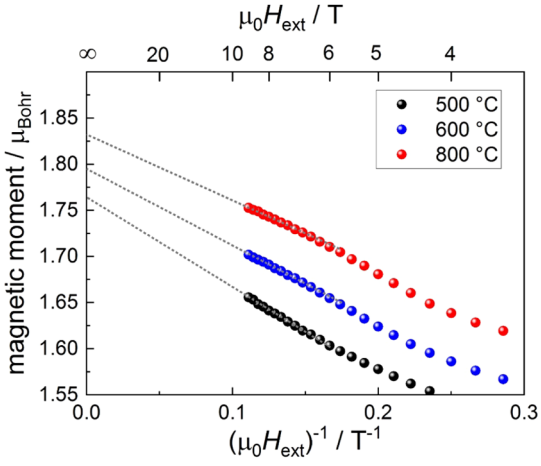


Figure 9. High-field magnetization plotted as a function of $1/\mu_0 H$. The dashed lines represent extrapolations of the high-field behavior.

Depending on the preparation temperature, the coefficients a_1 and a_2 exhibit different behaviors (see the inset of Figure 10). Whereas a_1 is almost constant or moderately increasing toward 800 °C, a_2 drops by a factor of 4 for the specimen prepared at 800 °C, indicating that crystal anisotropy decreases with the preparation temperature. This finding is in line with the results of the analysis of the anisotropy work experiment. The observation that a_1 is mildly growing for the sample

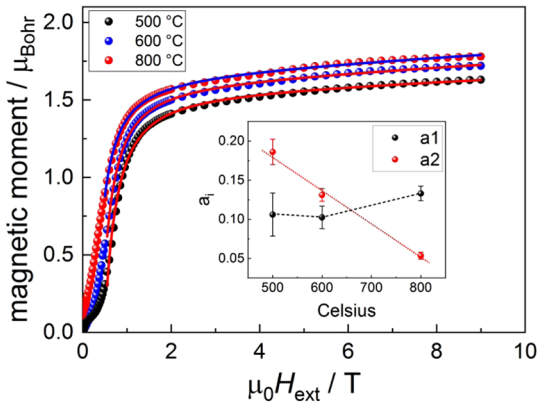


Figure 10. Fit of eq 2 to the high-field magnetizations (per fu) ("law of approach") considering the terms $\propto 1/(\mu_0 H)$ and $\propto 1/(\mu_0 H)^2$ (solid lines). The temperature dependence of the coefficients a_1 and a_2 is displayed in the inset.

prepared at 800 °C could possibly attribute to an increase of sulfur defects with increasing preparation temperature.

Next, we discuss the coercive fields (the inset of Figure 11) derived from the low-field hysteresis curves displayed in Figure

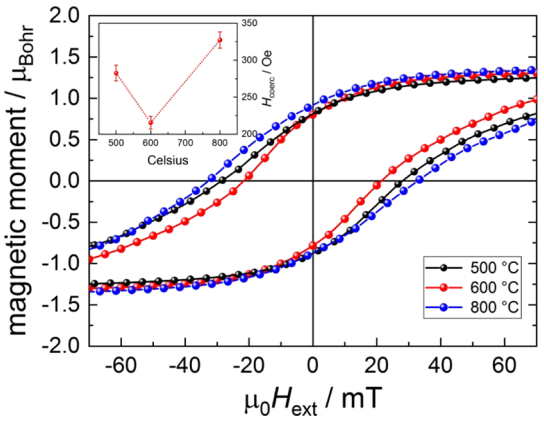


Figure 11. Low-field hysteresis curves at T = 4.2 K for the three samples prepared at the temperatures, as indicated. The upper inset shows the coercive field as a function of preparation temperature.

11. The coercive fields range between ~200 and ~350 Oe. However, they show a nonuniform behavior with the annealing temperature and after an initial drop from 500 to 600 °C, the coercive field increases again for the sample prepared at 800 °C. This parallels the behavior of the parameter a_1 of the law-of-approach fits (see the inset of Figure 10), indicating that the coercive field is primarily determined by inclusions, some disorder and/or microstrain, and less by anisotropy.

The dynamics of domain wall motion was studied by frequency-dependent magnetic susceptibility experiments. Figure 12 displays the real part of the ac susceptibilities measured at 1 kHz as a function of temperature between 50 and 200 K. As for the dc susceptibilities, there is no indication of unusual behavior at or around 60 K. With increasing preparation temperature, the ac susceptibilities increase. On approaching T_C, indicated by a peak and a steep decrease above, the susceptibilities exhibit a bulge, which we ascribed to dissipation due to domain reorientation dynamics, similarly seen in the imaginary part of the ac susceptibilities (inset b of the Figure 13).

https://doi.org/10.1021/acsomega.1c01412
ACS Omega 2021, 6, 13375−13383

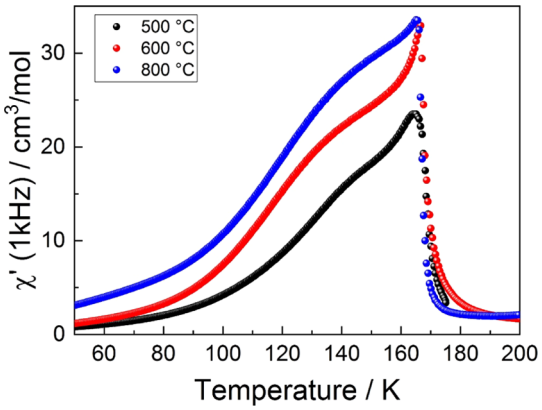


Figure 12. Real part of the ac susceptibilities collected at a frequency of 1 kHz.

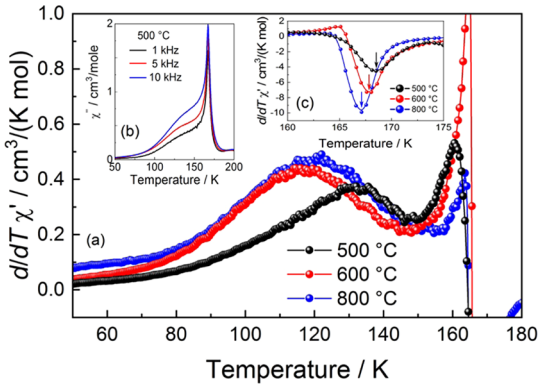


Figure 13. (a) Temperature derivatives of the real part, χ', of the ac susceptibilities taken at a frequency of 1 kHz. The inset (c) highlights the steep decrease above T_C. The arrows mark the positions of the minima, revealing a continuous downshift of T_C with increasing preparation temperature. (b) Imaginary part of the ac susceptibility of the 500 °C sample measured with frequencies of 1, 5, and 10 kHz, as indicated.

The bulge shifts nonlinearly with the preparation temperature as is well seen in the temperature derivative of the real part of the ac susceptibilities (Figure 13a). The maximum of the bulge is at the lowest temperature for the sample prepared at 600 °C, correlating with the behavior of the coercive fields (see the inset of Figure 11). The ferrimagnetic transition sharpens continuously with increasing preparation temperature. For identifying the minimum of the derivative $d\chi'/dT$ with T_C, the derivatives also reveal that by increasing the preparation temperature a steady, however minute downshift of T_C from 168.6(5) to 167.8(5) and 167.1(3) K takes place for sample preparation temperatures of 500, 600, and 800 °C, respectively.

CONCLUSIONS

$FeCr_2S_4$ samples synthesized by mechanochemistry methods followed by subsequent heat treatment led to nanocrystalline products exhibiting different domain size distributions. Increasing the preparation temperature generates larger coherently scattering domains and lower microstrain. dc and ac magnetic susceptibility investigations evidence a phase transition from paramagnetic to the ferrimagnetic state at a Curie temperature T_C of ∼ 167 K, slightly dependent on the preparation temperature. Above T_C, the magnetic susceptibility data significantly deviate from Curie−Weiss behavior, and only at temperatures high enough, the linear behavior of the inverse magnetization data is observed. This unusual observation is ascribed to the survival of easily polarizable spin clusters well above T_C. The *zfc*−*fc* curves show a bifurcation at distinct $T < T_C$, with T depending on the preparation temperatures of the samples. Below this bifurcation, the *zfc* data exhibit a sharp drop and reveal a magnetic anomaly at $T \sim 9$ K, which is related to the transition into the orbital ordered state. This transition is well pronounced for the 600 and 800 °C samples and less clearly visible for the 500 °C sample. It appears that the transition into the orbital ordered state is a local phenomenon and does not markedly depend on the size of coherently scattering domains. The analysis of the magnetization behavior of the samples at low temperatures as a function of magnetic field clearly reveals a relation between microstrain and different crystalline anisotropy energies. Such a relation also holds for the coercive fields. Domain dynamics and associated anomalies in the real parts of the ac susceptibilities are consistent with these findings.

EXPERIMENTAL SECTION

The samples were prepared by mechanochemical milling in a high energy planetary mill (Pulverisette 7, Fritsch, Idar-Oberstein, Germany). Stoichiometric amounts of the corresponding binary sulfides, FeS and Cr_2S_3, were filled in a zirconia grinding beaker furnished with six zirconia spheres with a diameter of 15 mm and milled at a rotational speed of 350 rpm for 6 h. To increase the crystallinity, the powders were subsequently annealed for 2 h in a tube furnace under flowing H_2S gas at temperatures of 500, 600, and 800 °C. FeS and Cr_2S_3 were prepared by a solid-state reaction from the elements, Fe, S, and Cr, respectively, in evacuated (10^{-4} mbar) and sealed silica ampoules. Due to the significant vapor pressure of sulfur, the sealed ampoules were first slowly heated up to 400 °C in 960 min and held at this temperature for 1440 min. The temperature then was increased to the final temperature of 1000 °C in 2880 min and held for 4320 min. After the reaction was complete, the ampoules were slowly cooled down to room temperature.

X-ray diffraction (XRPD) experiments were performed on a PANalytical Empyrean (Cu $K\alpha_{1,2}$), equipped with a PIXcel 1D detector using 0.1 mm outer diameter glass capillaries (Hilgenberg GmbH). Rietveld refinements were performed using TOPAS Academic software version 6.0.[66,67] To account for instrumental broadening, the profile function and axial divergence were determined using a LaB_6 standard sample (NIST 660c) measured under the same conditions. The mean domain size distribution was obtained by whole powder pattern modeling (WPPM) assuming a log-normal distribution $g(D)$ for the domain size according to[68,69]

$$g(D) = \frac{1}{D\sigma\sqrt{2\pi}} \exp\left[-\frac{1}{2}\left(\frac{\ln[D/\mu]}{\sigma}\right)^2\right] \quad (3)$$

where D is the domain size and μ and σ are the mean and variance, respectively.

In addition, the volume weighted average domain size (L_{vol}) and an upper-limit strain (ε_0 from the strain) were determined.[70,71]

Magnetic susceptibility measurements were performed by the extraction method in PPMS-9T system in a temperature range from 2 to 300 K and in magnetic fields up to 9 T.

https://doi.org/10.1021/acsomega.1c01412
ACS Omega 2021, 6, 13375−13383

AUTHOR INFORMATION

Corresponding Authors

Reinhard K. Kremer − *Max-Planck-Institut für Festkörperforschung, 70569 Stuttgart, Germany;* orcid.org/0000-0001-9062-2361; Email: rekre@fkf.mpg.de

Wolfgang Bensch − *Christian-Albrechts-Universität zu Kiel, Institut für Anorganische Chemie, 24118 Kiel, Germany;* orcid.org/0000-0002-3111-580X; Email: wbensch@ac.uni-kiel.de

Authors

Anna-Lena Hansen − *Christian-Albrechts-Universität zu Kiel, Institut für Anorganische Chemie, 24118 Kiel, Germany; Institute for Applied Materials—Energy Storage Systems—IAM-ESS, Karlsruhe Institute of Technology—KIT, 76344 Eggenstein-Leopoldshafen, Germany*

Eva M. Heppke − *Technische Universität Berlin, Fakultät II, Institut für Chemie, 10623 Berlin, Germany*

Martin Lerch − *Technische Universität Berlin, Fakultät II, Institut für Chemie, 10623 Berlin, Germany;* orcid.org/0000-0002-4065-4928

Complete contact information is available at: https://pubs.acs.org/10.1021/acsomega.1c01412

Notes

The authors declare no competing financial interest.

ACKNOWLEDGMENTS

Financial support by the State of Schleswig-Holstein is gratefully acknowledged. Maren Rasmussen and Henning Lühmann are gratefully acknowledged for technical support with PPMS measurements.

REFERENCES

(1) Xu, J.; Zheng, X.; Yang, S.; Xi, L.; Wang, S.; Zhang, L.; Yang, W.; Yang, J.; Ma, X.; Chen, D.; He, L.; Deng, S.; Zhang, J.; Wu, Y.; Shen, B. Large Linear Negative Thermal Expansion in NiAs-type Magnetic Intermetallic Cr−Te−Se Compounds. *Inorg. Chem.* **2020**, *59*, 8603−8608.

(2) Zhang, T.; Su, X.; Yan, Y.; Liu, W.; You, Y.; Xie, H.; Yang, D.; Uher, C.; Tang, X. Structure and thermoelectric properties of 2D $Cr_2Se_{3-3x}S_{3x}$ solid solutions. *J. Mater. Chem. C* **2018**, *6*, 836−846.

(3) Pisharody, K. R. Thermoelectric properties of chromium sulfoselenides. *J. Solid State Chem.* **1979**, *30*, 149−156.

(4) Hansen, A.-L.; Dankwort, T.; Groß, H.; Etter, M.; König, J.; Duppel, V.; Kienle, L.; Bensch, W. Structural properties of the thermoelectric material $CuCrS_2$ and of deintercalated Cu_xCrS_2 on different length scales: X-ray diffraction, pair distribution function and transmission electron microscopy studies. *J. Mater. Chem. C* **2017**, *5*, 9331−9338.

(5) Guo, Q.; Berthebaud, D.; Ueda, J.; Tanabe, S.; Miyoshi, A.; Maeda, K.; Mori, T. Facile p−n control, and magnetic and thermoelectric properties of chromium selenides $Cr_{2+x}Se_3$. *J. Mater. Chem. C* **2019**, *7*, 8269−8276.

(6) Liu, Y.; Abeykoon, M.; Stavitski, E.; Attenkofer, K.; Petrovic, C. Magnetic anisotropy and entropy change in trigonal Cr_5Te_8. *Phys. Rev. B* **2019**, *100*, No. 245114.

(7) Ho, C.-H.; Lai, X.-R. Effect of Cr on the Structure and Property of $Mo_{1-x}Cr_xSe_2$ ($0 \le x \le 0.2$) and Cr_2Se_3. *ACS Appl. Electron. Mater.* **2019**, *1*, 370−378.

(8) Wontcheu, J.; Bensch, W.; Wilkening, M.; Heitjans, P.; Indris, S.; Sideris, P.; Grey, C. P.; Mankovsky, S.; Ebert, H. Tuning the structural and physical properties of $Cr_2Ti_3Se_8$ by Lithium intercalation: A Study of the Magnetic Properties, Investigation of Ion Mobility with NMR Spectroscopy and Electronic Band Structure Calculations. *J. Am. Chem. Soc.* **2008**, *130*, 288−299.

(9) Chu, J.; Zhang, Y.; Wen, Y.; Qiao, R.; Wu, C.; He, P.; Yin, L.; Cheng, R.; Wang, F.; Wang, Z.; Xiong, J.; Li, Y.; He, J. Submillimeter-Scale Growth of One-Unit-Cell-Thick Ferrimagnetic Cr_2S_3 Nanosheets. *Nano Lett.* **2019**, *19*, 2154−2161.

(10) Krengel, M.; Hansen, A.-L.; Hartmann, F.; van Dinter, J.; Bensch, W. Elucidation of the Sodium − Copper Extrusion Mechanism in $CuCrS_2$: A High Capacity, Long-life Anode Material for Sodium Ion Batteries. *Batteries Supercaps* **2018**, *1*, 176−183.

(11) Groß, H.; Dankwort, T.; Hansen, A.-L.; Schürmann, U.; Duppel, V.; Poschmann, M.; Meingast, A.; Groeneveld, D.; König, J.; Bensch, W.; Kienle, L. Purification by SPS and formation of a unique 3D nanoscale network: The showcase of Ni-Cr-S. *J. Mater. Chem. C* **2019**, *7*, 15188−15196.

(12) Bertinshaw, J.; Ulrich, C.; Günther, A.; Schrettle, F.; Wohlauer, M.; Krohns, S.; Reehuis, M.; Studer, A. J.; Avdeev, M.; Quach, D. V.; Groza, J. R.; Tsurkan, V.; Loidl, A.; Deisenhofer, J. $FeCr_2S_4$ in magnetic fields: possible evidence for a multiferroic ground state. *Sci. Rep.* **2015**, *4*, No. 6079.

(13) Lin, L.; Zhu, H. X.; Jiang, X. M.; Wang, K. F.; Dong, S.; Yan, Z. B.; Yang, Z. R.; Wan, J. G.; Liu, J.-M. Coupled ferroelectric polarization and magnetization in spinel $FeCr_2S_4$. *Sci. Rep.* **2015**, *4*, No. 6530.

(14) Strinić, A.; Reschke, S.; Vasin, K. V.; Schmidt, M.; Loidl, A.; Tsurkan, V.; Eremin, M. V.; Deisenhofer, J. Magnetoelectric properties and low-energy excitations of multiferroic $FeCr_2S_4$. *Phys. Rev. B* **2020**, *102*, No. 134409.

(15) Shirane, G.; Cox, D. E.; Pickart, S. J. Magnetic Structures in $FeCr_2S_4$ and $FeCr_2O_4$. *J. Appl. Phys.* **1964**, *35*, 954−955.

(16) Haacke, G.; Beegle, L. C. Electrical Transport in $FeCr_2S_4$-$CuCr_2S_4$ Spinels. *J. Appl. Phys.* **1968**, *39*, 656−657.

(17) Goldstein, L.; Lyons, D. H.; Gibart, P. Anisotropic resistivity and anisotropic magnetoresistance of the magnetic semiconductor $FeCr_2S_4$. *Solid State Commun.* **1973**, *13*, 1503−1506.

(18) Hoy, G. R.; Chandra, S. Effective Field Parameters in Iron Mössbauer Spectroscopy. *J. Chem. Phys.* **1967**, *47*, 961−965.

(19) Eibschutz, M.; Shtrikman, S.; Tenenbaum, Y. Magnetically induced electric field gradient in tetrahedral divalent iron: $FeCr_2S_4$. *Phys. Lett. A* **1967**, *24*, 563−564.

(20) Spender, M. R.; Morrish, A. H. Mössbauer Study of the Ferrimagnetic Spinel $FeCr_2S_4$. *Can. J. Phys.* **1972**, *50*, 1125−1138.

(21) Spender, M. R.; Morrish, A. H. A low temperature transition in $FeCr_2S_4$. *Solid State Commun.* **1972**, *11*, 1417−1421.

(22) van Diepen, A. M.; van Stapele, R. P. Ordered local distortions in cubic $FeCr_2S_4$. *Solid State Commun.* **1973**, *13*, 1651−1653.

(23) Lotgering, F. K.; van Diepen, A. M.; Olijhoek, J. F. Mössbauer spectra of iron-chromium sulphospinels with varying metal ratio. *Solid State Commun.* **1975**, *17*, 1149−1153.

(24) Tsurkan, V.; Fritsch, V.; Hemberger, J.; Krug Von Nidda, H.-A.; Samusi, D.; Körner, S.; Scheidt, E.-W.; Horn, S.; Tidecks, R.; Loidl, A.; et al. Orbital fluctuations and orbital order in $FeCr_2S_4$. *J. Phys. Chem. Solids* **2005**, *66*, 2036−2039.

(25) Ramirez, A. P.; Cava, R. J.; Krajewski, J. Colossal magnetoresistance in Cr-based chalcogenide spinels. *Nature* **1997**, *386*, 156−159.

(26) Nath, A.; Klencsar, Z.; Kuzmann, E.; Homonnay, Z.; Vertes, A.; Simopoulos, A.; Devlin, E.; Kallias, G.; Ramirez, A. P.; Cava, R. J. Nanoscale magnetism in the chalcogenide spinel $FeCr_2S_4$: Common origin of colossal magnetoresistivity. *Phys. Rev. B* **2002**, *66*, No. 212401.

(27) Chen, Z.; Tan, S.; Yang, Z.; Zhang, Y. Evidence for a non-double-exchange mechanism in $FeCr_2S_4$. *Phys. Rev. B* **1999**, *59*, 11172−11174.

(28) Chiuzbăian, S. G.; Brignolo, S.; Hague, C. F.; Delaunay, R.; Guarise, M.; Nicolaou, A.; Yang, Z.; Zhou, H.; Mariot, J.-M. Spectroscopic Evidence for Superexchange in the Ferrimagnetic Spinel $FeCr_2S_4$. *J. Phys. Chem. C* **2017**, *121*, 22369−22376.

(29) Gibart, P.; Dormann, J.-L.; Pellerin, Y. Magnetic Properties of $FeCr_2S_4$ and $CoCr_2S_4$. *Phys. Status Solidi B* **1969**, *36*, 187−194.
(30) Tsurkan, V.; Hemberger, J.; Klemm, M.; Klimm, S.; Loidl, A.; Horn, S.; Tidecks, R. Ac susceptibility studies of ferrimagnetic $FeCr_2S_4$ single crystals. *J. Appl. Phys.* **2001**, *90*, 4639−4644.
(31) Dey, K.; Indra, A.; Giri, S. Critical behavior of multiferroic sulpho spinel compounds: MCr_2S_4 (M = Co & Fe). *J. Alloys Compd.* **2017**, *726*, 74−80.
(32) Büttgen, N.; Hemberger, J.; Fritsch, V.; Krimmel, A.; Mücksch, M.; Krug von Nidda, H.-A.; Lunkenheimer, P.; Fichtl, R.; Tsurkan, V.; Loidl, A. Orbital physics in sulfur spinels: ordered, liquid and glassy ground states. *New J. Phys.* **2004**, *6*, No. 191.
(33) Tsurkan, V.; Baran, M.; Szymczak, R.; Szymczak, H.; Tidecks, R. Spin-glass like states in the ferrimagnet $FeCr_2S_4$. *Phys. B* **2001**, *296*, 301−305.
(34) Shen, C.; Yang, Z.; Tong, R.; Li, G.; Wang, B.; Sun, Y.; Zhang, Y. Magnetic anisotropy-induced spin-reorientation in spinel $FeCr_2S_4$. *J. Magn. Magn. Mater.* **2009**, *321*, 3090−3092.
(35) Tong, R.; Yang, Z.; Shen, C.; Zhu, X.; Sun, Y.; Li, L.; Zhang, S.; Pi, L.; Qu, Z.; Zhang, Y. Disorder-induced orbital glass state in $FeCr_2S_4$. *Europhys. Lett.* **2010**, *89*, No. 57002.
(36) Tsurkan, V.; Fita, I.; Baran, M.; Puzniak, R.; Samusi, S.; Szymczak, R.; Szymczak, H.; Klimm, S.; Klemm, M.; Horn, S.; Tidecks, R. Effect of pressure on the magnetic and transport properties of the ferrimagnetic semiconductor $FeCr_2S_4$. *J. Appl. Phys.* **2001**, *90*, 875−881.
(37) Broquetas Colominas, C.; Ballestracci, R.; Roult, G. Étude par diffraction neutronique du spinelle $FeCr_2S_4$. *J. Phys.* **1964**, *25*, 526−528.
(38) Kim, S. J.; Kim, W. C.; Kim, C. S. Neutron diffraction and Mössbauer studies on $Fe_{1-x}Cr_2S_4$ (x = 0.0, 0.04, 0.08). *J. Appl. Phys.* **2002**, *91*, 7935−7937.
(39) Göbel, H. Local Lattice Distortions in Chromium Chalcogenide Spinels at Low Temperatures. *J. Magn. Magn. Mater.* **1976**, *3*, 143−146.
(40) Mertinat, M.; Tsurkan, V.; Samusi, D.; Tidecks, R.; Haider, F. Low-temperature structural transition in $FeCr_2S_4$. *Phys. Rev. B* **2005**, *71*, No. 100408.
(41) Maurer, D.; Tsurkan, V.; Horn, S.; Tidecks, R. Ultrasonic study of ferrimagnetic $FeCr_2S_4$: Evidence for low temperature structural transformations. *J. Appl. Phys.* **2003**, *93*, 9173−9176.
(42) Kalvius, G. M.; Krimmel, A.; Hartmann, O.; Wäppling, R.; Wangner, F. E.; Litterst, F. J.; Tsurkan, V.; Loidl, A. Low temperature incommensurately modulated and noncollinear spin structure in $FeCr_2S_4$. *J. Phys.: Condens. Matter* **2010**, *22*, No. 052205.
(43) Ito, M.; Nagi, Y.; Kado, N.; Urakawa, S.; Ogawa, T.; Kondo, A.; Koyama, K.; Watanabe, K.; Kindo, K. Magnetic properties of spinel $FeCr_2S_4$ in high magnetic field. *J. Magn. Magn. Mater.* **2011**, *323*, 3290−3293.
(44) Felea, V.; Yasin, S.; Günther, A.; Deisenhofer, J.; Krug von Nidda, H.-A.; Scheidt, E.-W.; Quach, D. V.; Groza, J. R.; Zherlitsyn, S.; Tsurkan, V.; Lemmens, P.; Wosnitza, J.; Loidl, A. Ultrasound study of $FeCr_2S_4$ in high magnetic fields. *J. Phys.: Condens. Matter* **2014**, *26*, No. 486001.
(45) Feiner, L. F. Unified description of the cooperative Jahn-Teller effect in $FeCr_2S_4$ and the impurity Jahn-Teller effect in $CoCr_2S_4$:Fe^{2+}. *J. Phys. C: Solid State Phys.* **1982**, *15*, 1515−1524.
(46) Brossard, L.; Dormann, J.; Goldstein, L.; Gibart, P.; Renaudin, P. Second-order phase transition in $FeCr_2S_4$ investigated by Mössbauer spectroscopy: An example of orbital para-to-ferromagnetism transition. *Phys. Rev. B* **1979**, *20*, 2933−2944.
(47) Fichtl, R.; Tsurkan, V.; Lunkenheimer, P.; Hemberger, J.; Fritsch, V.; Krug von Nidda, H.-A.; Scheidt, E.-W.; Loidl, A. Orbital Freezing and Orbital Glass State in $FeCr_2S_4$. *Phys. Rev. Lett.* **2005**, *94*, No. 027601.
(48) Tsurkan, V.; Zaharko, O.; Schrettle, F.; Kant, Ch.; Deisenhofer, J.; Krug von Nidda, H.-A.; Felea, V.; Lemmens, P.; Groza, J. R.; Quach, D. V.; Gozzo, F.; Loidl, A. Structural anomalies and the orbital ground state in $FeCr_2S_4$. *Phys. Rev. B* **2010**, *81*, No. 184426.
(49) Shen, C.; Yang, Z.; Tong, R.; Zi, Z.; Song, W.; Sun, Y.; Pi, L.; Zhang, Y. Magnetic anomaly around orbital ordering in $FeCr_2S_4$. *J. Appl. Phys.* **2011**, *109*, No. 07E144.
(50) Zestrea, V.; Kodash, V. Y.; Felea, V.; Petrenco, P.; Quach, D. V.; Groza, J. R.; Tsurkan, V. Structural and magnetic properties of $FeCr_2S_4$ spinel prepared by field-activated sintering and conventional solid-state synthesis. *J. Mater. Sci.* **2008**, *43*, 660−664.
(51) Zub, E. M. Electrical and galvanomagnetic properties of films of $FeCr_2S_4$, $CuCr_2S_4$, and $Cu_{0.3}Fe_{0.7}Cr_2S_4$. *Inorg. Mater.* **1983**, *19*, 133−135.
(52) Riedel, E.; Karl, R. Mössbauer studies of thiospinels. IV. The system $FeCr_2S_4$-Fe_3S_4. *J. Solid State Chem.* **1981**, *38*, 48−54.
(53) Riedel, E.; Al-Juani, A.; Rackwitz, R.; Sochtig, H. Röntgenographische und elektrische Eigenschaften, Mößbauer- und IR-Spektren des Systems $FeCr_2(S_{1-x}Se_x)_4$. *Z. Anorg. Allg. Chem.* **1981**, *480*, 49−59.
(54) Lotgering, F. K. On The Ferrimagnetism of some Sulphides and Oxides. *Philips Res. Rep.* **1956**, *11*, 190−249.
(55) Kurmaev, E. Z.; Postnikov, A. V.; Palmer, H. M.; Greaves, C.; Bartkowski, St.; Tsurkan, V.; Demeter, M.; Hartmann, D.; Neumann, M.; Zatsepin, D. A.; Galakhov, V. R.; Shamin, S. N.; Trofimova, V. Electronic structure of $FeCr_2S_4$ and $Fe_{0.5}Cu_{0.5}Cr_2S_4$. *J. Phys.: Condens. Matter* **2000**, *12*, 5411−5421.
(56) Diehm, P. M.; Agoston, P.; Albe, K. Size-Dependent Lattice Expansion in Nanoparticles: Reality or Anomaly? *ChemPhysChem* **2012**, *13*, 2443−2454.
(57) Wasserman, H. J.; Vermaak, S. J. On the determination of the surface stress of copper and platinum. *Surf. Sci.* **1972**, *32*, 168−174.
(58) Sharma, M.; Murugavel, S.; Shukla, D. K.; De Groot, F. M. F. Reversal in the Lattice Contraction of α-Fe_2O_3 Nanoparticles. *J. Phys. Chem. C* **2018**, *122*, 9292−9301.
(59) Park, M. S.; Kwon, S. K.; Youn, S. J.; Min, B. I. Half-metallic electronic structures of giant magnetoresistive spinels: $Fe_{1-x}Cu_xCr_2S_4$ (x=0.0,0.5,1.0). *Phys. Rev. B* **1999**, *59*, 10018−10024.
(60) Sarkar, S.; Maitra, T.; Valentí, R.; Saha-Dasgupta, T. Comparative study of $FeCr_2S_4$ and $FeSc_2S_4$: Spinels with orbitally active A site. *Phys. Rev. B* **2010**, *82*, No. 041105.
(61) Cullity, B. D.; Graham, C. D. *Introduction to Magnetic Materials*; John Wiley & Sons, Inc.: Hoboken, New Jersey, 2009.
(62) Kronmüller, H.; Grimm, H. High-field susceptibility and spin-wave spectrum of $Fe_{40}Ni_{40}P_{14}B_6$-alloys. *J. Magn. Magn. Mater.* **1977**, *6*, 57−60.
(63) Grimm, H.; Kronmüller, H. Magnetic polarization of amorphous alloys in the approach to ferromagnetic saturation. *J. Magn. Magn. Mater.* **1980**, *15*−*18*, 1411−1412.
(64) Kronmüller, H.; Lenge, N.; Habermeier, H.-U. Investigation of the approach to ferromagnetic saturation in sputtered amorphous $Fe_{80-x}Ni_xB_{20}$ films. *Phys. Lett. A* **1984**, *101*, 439−442.
(65) Lenge, N.; Kronmüller, H. Low temperature magnetization of sputtered amorphous Fe-Ni-B films. *Phys. Status Solidi A* **1986**, *95*, 621−633.
(66) Rietveld, H. M. A profile refinement method for nuclear and magnetic structures. *J. Appl. Crystallogr.* **1969**, *2*, 65−71.
(67) Coelho, A. A. *Topas Academic* (Version 6), Australia, 2016.
(68) Scardi, P.; Leoni, M. Whole powder pattern modelling. *Acta Crystallogr., Sect. A: Found. Crystallogr.* **2002**, *58*, 190−200.
(69) Scardi, P.; Leoni, M. *Diffraction Analysis of the Microstructure of Materials*; Mittemeijer, E. J.; Scardi, P., Eds.; Springer: Berlin, 2004; pp 51−91.
(70) Balzar, D.; Audebrand, N.; Daymond, M. R.; Fitch, A.; Hewat, A.; Langford, J. I.; Le Bail, A.; Louër, D.; Masson, O.; McCowan, C. N.; et al. Size−strain line-broadening analysis of the ceria round-robin sample. *J. Appl. Crystallogr.* **2004**, *37*, 911−924.
(71) Snyder, L. R.; Fiala, J.; Bunge, H.-J. *Defect and Microstructure Analysis by Diffraction*; Oxford University Press: Oxford, New York, 1999.

https://doi.org/10.1021/acsomega.1c01412
ACS Omega 2021, 6, 13375−13383